In Situ ESEM Investigation of KCl-Induced Corrosion of a FeCrAl and a Model FeNiCrAl Alloy in Lab Air at 450 degrees C

OPEN ACCESS

In Situ ESEM Investigation of KCl-Induced Corrosion of a FeCrAl and a Model FeNiCrAl Alloy in Lab Air at 450°C

In Situ ESEM Investigation of KCl-Induced Corrosion of a FeCrAl and a Model FeNiCrAl Alloy in Lab Air at 450°C

N. Mortazavi,[a,z] L. Intiso,[a,b] N. Israelsson,[c] L.-G. Johansson,[c] and M. Halvarsson[a]

[a]*Department of Applied Physics, Chalmers University of Technology, SE-412 96 Gothenburg, Sweden*
[b]*Centro Sviluppo Materiali S.p.A, 00128 Rome, Italy*
[c]*Department of Chemistry and Chemical Engineering, High Temperature Corrosion Centre (HTC), Chalmers University of Technology, SE-412 96 Gothenburg, Sweden*

The very early stages of KCl-induced corrosion of a FeCrAl and a FeNiCrAl alloy in an O_2/H_2O environment were studied using in-situ Environmental Scanning Electron Microscopy (ESEM). The samples were KCl contaminated and then exposed to lab air at a total pressure of 4.8 Torr at 450°C. After exposure, the samples were analyzed using SEM-EDX, FIB and STEM-EDX. For both alloys, fast oxide growth occurred at the KCl particles. Far away from the KCl particles, a thin base oxide formed with potassium chromate nodules on top. The base oxide was layered, consisting of iron-chromium oxide on top and alumina in the bottom part. The FeCrAl alloy suffered internal oxidation while the FeNiCrAl did not. Both alloys formed sub-scale chlorides. A mechanism is proposed for the reaction of KCl on the surface and for the formation of different surface features at the KCl particles.
 [DOI: 10.1149/2.0581514jes]

Manuscript submitted August 3, 2015; revised manuscript received September 30, 2015. Published October 9, 2015.

The production of electricity in boilers fired by biomass and municipal waste is increasing, especially in Europe, contributing to a sustainable energy system.[1–3] In comparison to coal-fired plants, the fireside environment in biomass and waste-fired boilers is relatively high in alkali salts (NaCl and KCl) and low in sulfur. Because of the chemical composition of the flue gases, several components, e.g. the steam superheater tubes, which are made from heat resistant steels, suffer relatively severe corrosion.[4–9] Presently, low alloy steels and chromia-forming steels and alloys are used in these applications. However, alumina-forming high temperature materials may have a potential in these applications, either as solid materials (FeNiCrAl alloys) or as coatings (e.g., FeCrAl alloys). Thus, unlike chromia scales,[10–14] alumina scales are not expected to react rapidly with alkali chloride in the fireside environment. However, alumina-forming high temperature materials are usually used at relatively high temperature (typically 800–1250°C[15–17]) compared to boiler applications (<650°C). This is partly because the alloys are designed to form highly protective α-alumina scales, which need high temperatures to form.

In a study conducted done by Israelsson et al.,[18] the corrosion resistance of a ferritic FeCrAl alloy was investigated in a commercial waste fired boiler for 1000 h at 600°C and 700°C. It was reported that the FeCrAl alloy showed considerably better corrosion resistance than a high-alloy austenitic stainless steel, which is a good representative of chromia forming alloys that are currently used in waste fired boilers. Another alternative can be austenitic alumina forming FeNiCrAl alloys. These types of alloys have better mechanical properties than the ferritic ones and are of interest in many high-temperature applications, including biomass- and waste-fired boilers. Even though there have been several studies concern long term oxidation resistance of alumina-forming alloys,[16,19–21] only a few investigations have been devoted to the very initial stages of the oxidation process[22] and attempts to pursue dynamic experiments at low temperature are scarce.

In-situ high temperature oxidation using an Environmental Scanning Electron Microscope (ESEM), combining exposures with simultaneous imaging, is useful for investigating the initial stages of oxidation processes.[23–27] In the ESEM, various gases, temperatures and relative humidity can be present in the pressure range 1–10 Torr. By changing gas composition and temperature, different environments can be achieved in the ESEM chamber. As a result, the oxidation behavior of materials can be investigated by monitoring the formation of corrosion products as it occurs, at high magnification. A detailed description of in-situ ESEM exposures can be found in Refs. 24–26.

Working with iron, Jonsson et al.[23] showed that the in-situ ESEM oxidation behavior at 500°C was very close to that observed in well-controlled thermo-gravimetric (TG) exposures. The authors showed the great potential of in-situ exposures regarding quality and reproducibility. The in-situ ESEM technique has also been employed to investigate the KCl induced high temperature corrosion of a Fe-2.25Cr-1Mo at 400°C.[28] It was shown that Cl was transported through the scale by grain boundary transport and accumulated at the alloy/scale interface.

The aim of this study was to investigate the early stages of KCl-induced corrosion of two alumina forming alloys, austenitic FeNiCrAl (TH1, model alloy) and ferritic FeCrAl (Kanthal APMT) by means of in-situ ESEM exposures. Reference exposures were performed in a tube furnace at ambient pressure. Microstructural analyses were carried out after the exposures in order to investigate the formation of oxide scales by means of Focused Ion Beam (FIB) milling, Scanning Electron Microscopy (SEM), Energy Dispersive X-ray analysis (EDX) and Scanning Transmission Electron Microscopy (STEM).

Experimental

Sample preparation.— The alloys investigated were a commercial ferritic FeCrAl alloy (Kanthal APMT) and an austenitic FeCrNiAl model alloy (TH1), produced by advanced powder metallurgy and casting, respectively. The samples were supplied by Sandvik Heating Technology, Sweden. Table I shows the nominal chemical composition of the two alloys. The as-received materials were cut to produce coupons with the dimensions of 3 × 3 × 2 mm^3, using a low-speed saw in order to fit into the heating stage sample holder used for the in-situ ESEM exposures. The coupons were ground up to 4000 grit using SiC paper and then polished using diamond paste down to 1 μm. All samples were cleaned thoroughly in acetone and ethanol using an ultrasonic bath. The samples were then KCl contaminated by spraying with a saturated solution of KCl in water/ethanol (20:80) and then dried with cool air.

In-situ ESEM exposures.— The in-situ exposures were performed at 450°C in an FEI Quanta 200 Field Emission Gun (FEG) ESEM in ESEM mode using laboratory air at a pressure of 4.8 torr. The ESEM

Table I. Composition (at. %) of alloys TH1 and Kanthal APMT.

	Fe	Cr	Ni	Al	Mn	Mo	Si	C	RE
Kanthal APMT	Bal.	21.1		9.5	≤0.4	1.6	≤1.1	≤0.3	Hf, Y, Zr
TH1	18	19	Bal.	9.2					Hf, Y

[z]E-mail: nooshin.mortazavi@chalmers.se

has a temperature control unit coupled with a heating stage, which consists of a furnace and a thermocouple together with a water-cooling system. During imaging, the emitted secondary electrons (SEs) interact with the gas molecules in the chamber to produce (a) an electron cascade effect amplifying the SE-signal and (b) positively charged ions.

These ions are drawn toward the negatively charged sample surface where they neutralize the charging of the sample. A ramp-up speed of 50°C/min was chosen in this study. While imaging in ESEM-mode, a high accelerating voltage (30 kV) was used to increase the spatial resolution and to minimize the primary beam interaction with the gas inside the chamber. Details regarding temperature calibration of the heating stage are provided in Ref. 29.

Isothermal reference exposures.— In order to evaluate the in-situ ESEM exposures, reference exposures were performed in a horizontal tube furnace fitted with a silica tube at 450°C for 1 hour in laboratory air at ambient pressure. The net flow rate was 200 ml/min at NTP, corresponding to an average net gas velocity of 0.2 cm/s. The KCl sprayed samples were mounted on an alumina holder and put into the furnace. After the exposures, the samples were cooled in laboratory air and stored in a desiccator for further analyses.

Focused Ion Beam/Scanning Electron Microscope (FIB/SEM) workstation.— An FEI Versa 3D combined Focused Ion Beam and Scanning Electron Microscope (FIB/SEM) workstation was used to prepare and investigate cross-sections of the oxide scales formed and to perform site-specific preparation of thin foils for scanning transmission electron microscopy analysis, see below. For preparing thin foils, Pt was deposited on the surface to protect the oxide scale during the subsequent ion milling. For further details, see e.g. Refs. 30,31.

Scanning Electron Microscopy with Energy Dispersive X-rays spectroscopy (SEM-EDX).— The elemental composition of the oxide scales was determined using the high-vacuum mode in the FEI Quanta 200 FEG ESEM equipped with an Oxford Inca Energy Dispersive X-ray (EDX) system with a Silicon Drift Detector (SDD).

Scanning Transmission Electron Microscopy with EDX spectroscopy (STEM-EDX).— Scanning Transmission Electron Microscopy (STEM) was employed to acquire detailed microstructural information from the oxide layers and oxide/alloy interfaces. In this study, an FEI Titan 80–300 TEM/STEM equipped with a FEG operated at an accelerating voltage of 300 kV was used to create STEM images in Bright Field (BF) and High Angle Annular Dark Field (HAADF) modes. The instrument is equipped with an Oxford Inca EDX detector that was used for point and linescan analyses and for elemental mapping.

Results

In-situ ESEM exposures of TH1.— Fig. 1 shows a sequence of ESEM images acquired in-situ from a TH1 sample with added KCl after 6, 8, 14 and 60 minutes in lab air at 450°C. The typical size of the sprayed KCl particles was in the range 10–50 μm. Even during ramping the smaller KCl particles started to shrink and after 6 minutes at 450°C some of them had disappeared, leaving behind small oxide aggregates. One such remnant is seen in the upper left of the images. At this stage many of the remaining KCl crystals had developed oxide crusts and needle-like features, examples are seen in the middle and top part of the image acquired after 6 minutes. The needle-like crystals appear to grow from the salt/sample contact points. These features grew in size with time, reaching >20 μm at the end of the exposure (1 h).

After exposure the coordinates of the observed area were recorded and the sample was moved to the FIB/SEM for further analysis. Figure 2a shows the in-situ corroded alloy TH1 in SEM backscattered electron (BSE) mode. In addition to the oxide crust (to the right of the original position of the KCl particle), a thin base oxide had formed on the sample surface between the salt particles. The base

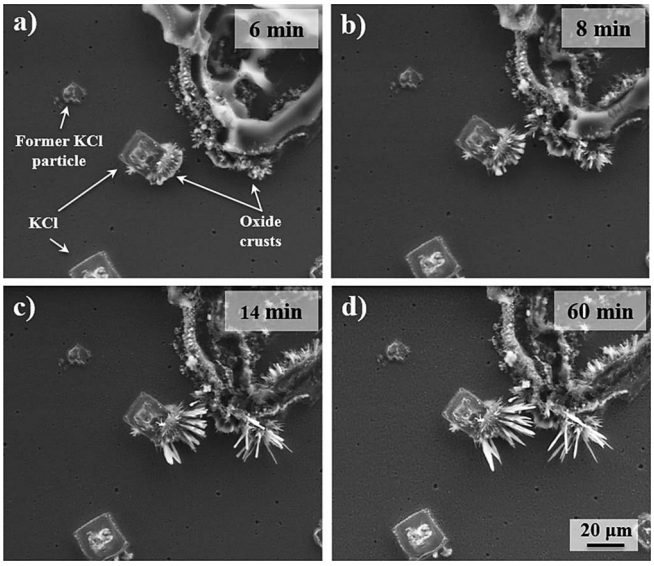

Figure 1. In-situ ESEM-SE micrographs obtained during the in-situ ESEM exposure of alloy TH1. After 6 minutes oxide structures developed around some of the salt particles (middle and top right), while others seemed to disappear quickly, leaving only traces of oxide at their original positions (upper left). (Lab air, up to 1 h, 450°C).

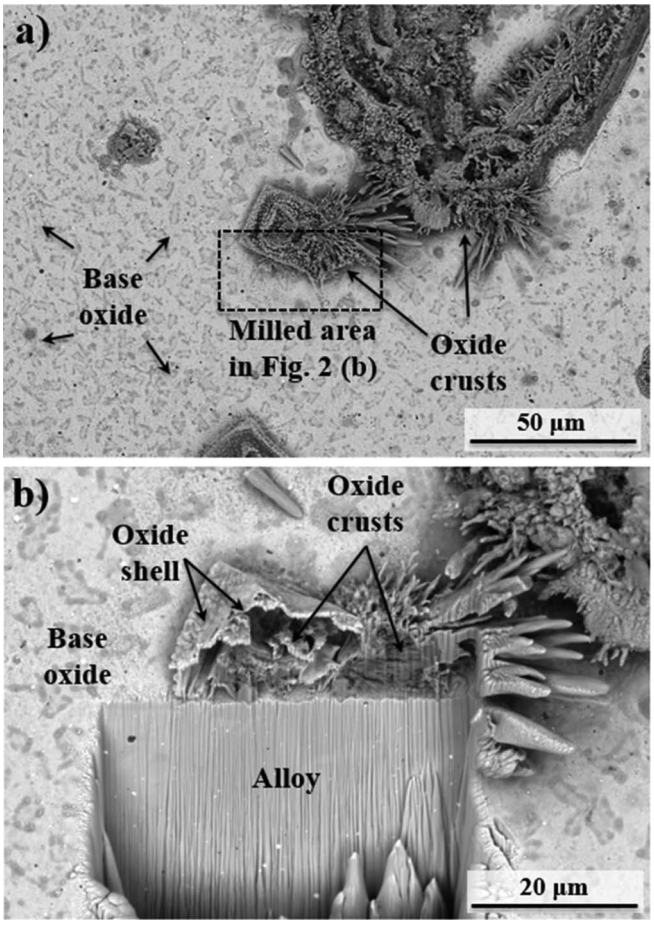

Figure 2. a) Plan view SEM-BSE micrograph of alloy TH1, b) SEM-BSE micrograph of FIB-milled cross-section (52° tilt) of the corroded salt particle visible in Fig. 2a after exposure in-situ in the ESEM. (Lab air, 1 h, 450°C).

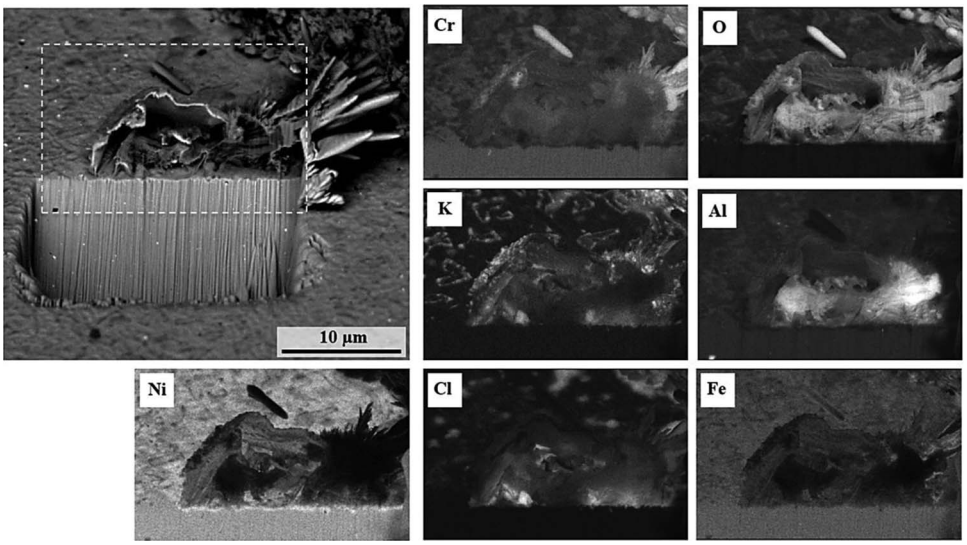

Figure 3. SEM-BSE micrograph and EDX maps of a FIB-milled cross section of alloy TH1. (In-situ exposure, lab air, 1 h, 450°C).

oxide consisted of a smooth oxide layer with numerous small nodules, darker in the SEM-BSE image. Figure 2b shows a FIB-milled cross-section of the boxed area in Fig. 2a. In this case no Pt-layer was used to protect the area of interest, as the oxide scale was much thicker than the depth of ion-beam damage. The image shows that the KCl particle has been replaced by a shell-like oxide feature that roughly mimics the shape of the former KCl particle. These features are termed *oxide shells*. In addition, there are oxide crusts both inside and outside the oxide shell. On the right hand side of the oxide shell and oxide crust, a cluster of needle-like objects can be seen (see also Fig. 2a).

SEM-EDX elemental maps were acquired from the cross-section in Fig. 2b and are presented in Fig. 3 together with an SEM-BSE micrograph at a tilt angle of 45°; a dashed rectangle indicates the analyzed area. The oxide shell mainly contained iron, aluminum and some chromium in addition to oxygen. On top of the oxide shell, potassium tended to be associated with chromium. These regions are interpreted as potassium chromate (K_2CrO_4), which has been reported to form in similar experiments.[32–36]

It may be noted that the potassium and chlorine maps overlap in some areas in the oxide crust inside the oxide shell. These areas are considered to correspond to unreacted KCl. The oxide crust, outside and inside the oxide shell, was dominated by aluminum and oxygen corresponding to aluminum oxide. The large needle-like features mainly contained Cr, Fe, O and around 10 at.% Cl, suggesting that they consisted of a mixture of chromium oxide, iron oxide and chromium/iron chloride.

The oxygen map shows bright areas on the alloy surface (above and to the left in the map). These areas correspond to the oxide nodules mentioned above (Fig. 2) and appear bright due to their greater thickness in comparison to the surrounding smooth base oxide. The base oxide was too thin to be accurately analyzed by SEM-EDX, but the nodules in the base oxide were thick enough to obtain some indications about their composition. They were enriched in Cr, also containing some Fe, while there was no significant Al content. The borders of the nodules were enriched in K, but not in Cl, indicating the presence of potassium chromate, K_2CrO_4. There were also remnants of KCl on the surface, corresponding to areas that are bright in both the K and Cl maps.

Beneath the oxide shell and the oxide crust, there was an oxidation-affected zone (OAZ) in the alloy substrate, which was depleted in Fe, Al and Cr, and enriched in Ni. The OAZ was < 1 µm deep. The nitrogen map (not shown) showed no indication of AlN in the alloy.

Figures 4a and 4b show SEM-SE and STEM bright-field (BF) images of a FIB-milled cross-section at a distance from the oxide shells and oxide crusts. The alloy, the base oxide, a nodule and the FIB-deposited Pt-layer are visible. The base oxide was very thin, in the order of 40 nm (4b) while the nodule was about 250 nm in thickness (4a). Beneath the oxide layer there was a 50–100 nm thick OAZ.

Figure 5a shows a STEM-HAADF cross-section image of alloy TH1, including the base oxide and a nodule. The nodule has a thickness of 150–250 nm and partly decomposed in the electron beam. Figure 5b shows STEM-BF cross-section images and STEM-EDX maps of the boxed area in Fig. 5a. The elemental maps show that the bottom

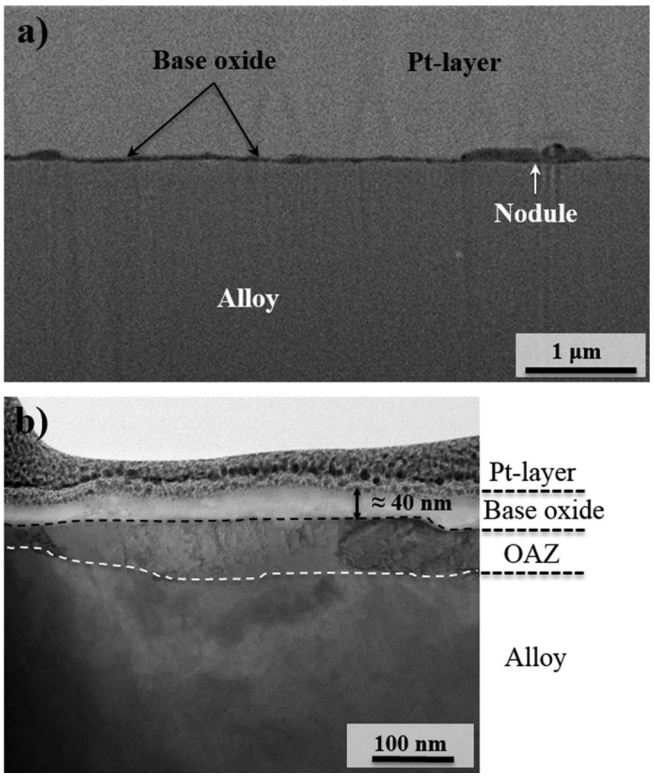

Figure 4. FIB-milled cross-section of the base oxide formed on alloy TH1; a) Overview SEM-SE micrograph showing the dark oxide scale beneath the brighter Pt-layer, b) STEM-BF image showing the oxide scale and the oxidation-affected zone in the alloy. (In-situ exposure, lab air, 1 h, 450°C).

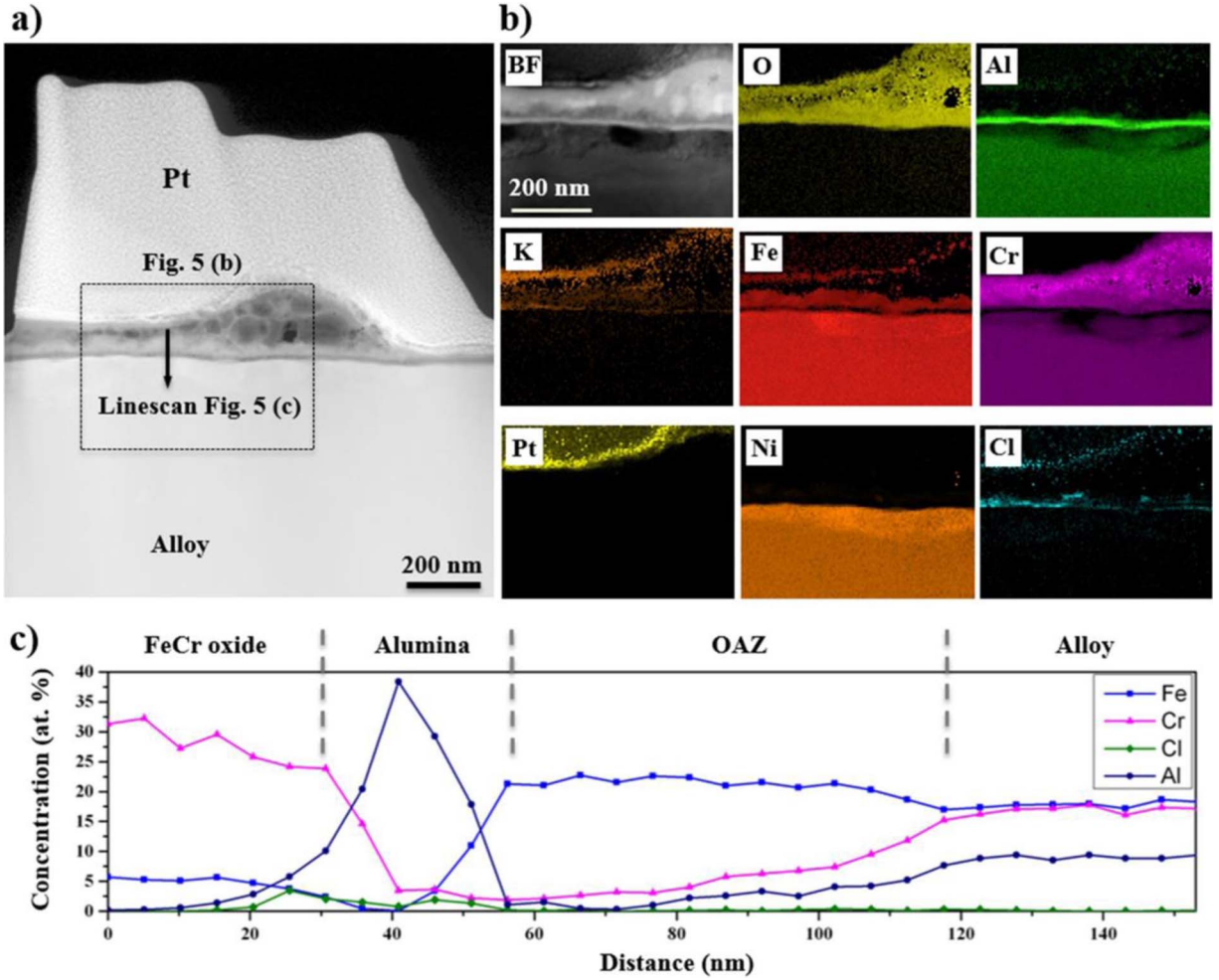

Figure 5. a) STEM-HAADF image acquired from alloy TH1, b) STEM-BF image and EDX maps, and c) STEM/EDX linescans across the oxide scale shown by an arrow in Fig. 5a. (In-situ exposure, lab air, 1 h, 450°C).

part of the base oxide consisted of a 10–20 nm thick, continuous alumina layer. On top of the alumina there is a 20–30 nm oxide layer containing both iron and chromium. The region outside of the iron chromium oxide was dominated by Cr, O and K and is interpreted as the product of decomposition of K_2CrO_4 in the electron beam (see discussion). Chlorine was detected both above and below the alumina layer. This was confirmed by a linescan performed through the base oxide (Fig. 5c). While the linescans showed small amounts of potassium in association with chlorine in these areas (not shown), the chlorine enrichments were mainly attributed to transition metal chloride. The EDX analysis shows that the OAZ beneath the base oxide was depleted in Al and Cr and consequently enriched in Fe and Ni. There was no sign of alloy nitridation.

In-situ ESEM exposures of Kanthal APMT.— Figure 6 shows an image sequence for Kanthal APMT exposed in-situ in the ESEM. The exposure procedure was the same as for TH1. Similar to alloy TH1, the surface morphology of Kanthal APMT was strongly affected at the location of the KCl particles. Already after 1 minute at 450°C, many of the small KCl particles had disappeared and oxide crusts had accumulated on some of the larger KCl particles. Images acquired after 2 minutes (not shown) indicated that KCl was being rapidly lost from the large salt particles. As a result of oxide crust formation and the disappearance of the KCl particles, oxide accumulations formed around the former KCl particles outlining the original shape of the

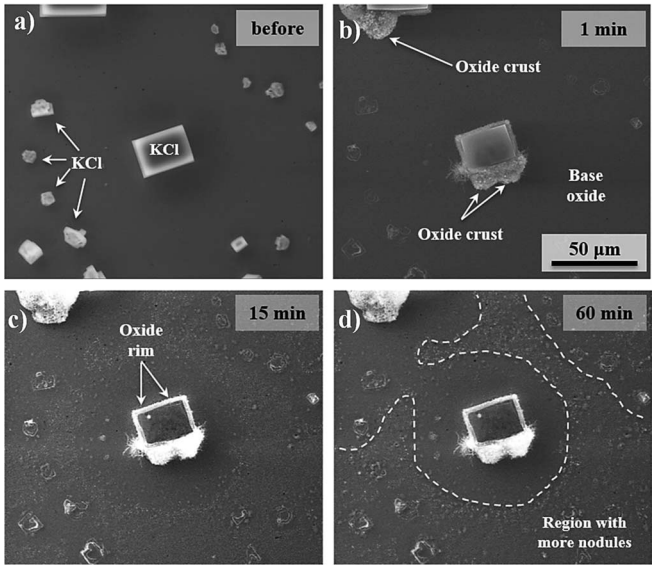

Figure 6. in-situ ESEM-SE micrographs obtained during in-situ ESEM exposure of alloy Kanthal APMT. The attention is drawn to the rapid disappearance of some KCl crystals. (Lab air, up to 1 h, 450°C).

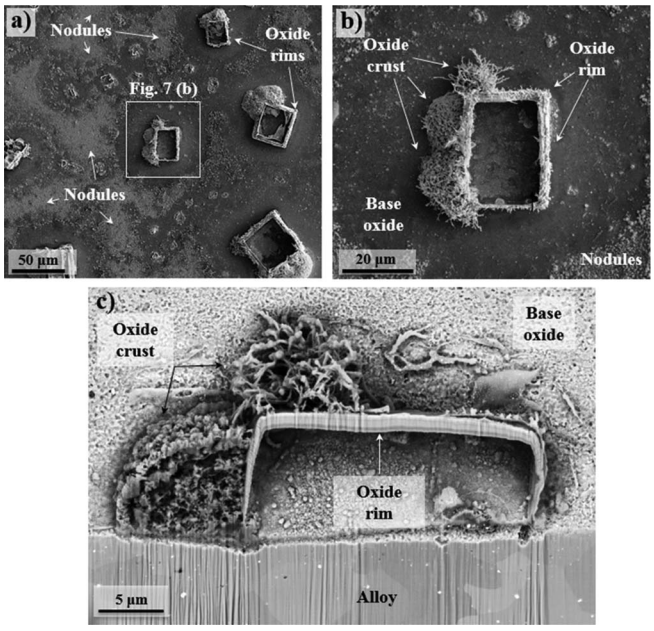

Figure 7. SEM-BSE micrographs of Kanthal APMT; a) plan view, b) boxed area in Fig. 7a in a higher magnification showing the thick oxide crust, and c) FIB-milled cross-section (52° tilt) through the former salt particle visible in Fig. 7b. Note that the image is rotated about 120° with respect to Fig. 7b. (in-situ exposure, lab air, 1 h, 450°C).

KCl particles. In contrast to the oxide shells observed on alloy TH1 (see above) the oxide accumulations on Kanthal APMT tended to have no "roof". Below, these features are termed '*oxide rims*'. At this stage nodules started to appear in the base oxide, forming halos around the former KCl particles. The nodules grew in size until the exposure was terminated (after 60 minutes).

After cooling to room temperature the sample was analyzed in the FIB/SEM. A plan view SEM-SE micrograph of the central area in Fig. 6 is shown in Figs. 7a and 7b (the image has been rotated about 120° with respect to Figure 6). On one side of the oxide rim (to the left in Figures 7a and 7b) a porous thick oxide crust with dendrites has formed outside the oxide rim. The base oxide next to the former KCl particle was thin and smooth, while some 20 µm away from the former KCl particle, the scale was thicker and covered by nodules.

A cross-section was prepared through the oxide crust and oxide rim in Fig. 7b and was investigated by SEM-BSE imaging, see Fig. 7c. The oxide rim, the base oxide, the porous crust on one side can be seen. It may be noted that the oxide rims formed on alloy Kanthal APMT were generally thicker than the oxide shells formed on alloy TH1. SEM-EDX elemental maps from the cross-section are shown in Fig. 8. There was little overlap of the Cl and K maps, confirming that KCl has fully reacted and/or volatilized at this stage. In the SEM-BSE image in Fig. 7c the oxide rim is seen to consist of layers with different brightness. The difference in brightness can be attributed to Z-contrast. Thus it appears that the oxide rim is layered and consists of iron, chromium and aluminum oxide. It may be noted that the inside of the oxide rim was subject to re-deposition during ion milling. Hence, the interpretation of those areas is problematic, see Ga map in Fig. 8.

The porous crust to the left of the oxide rim, rich in K, Cr and O, is attributed to potassium chromate, K_2CrO_4. Fig. 8 indicates that, in addition to potassium chromate, the interior of the porous crust contained oxides of iron, aluminum and chromium.

Low amounts of Cl and Mo ($\leq$2 at.% as measured by EDX) were detected at the metal/oxide interface below the oxide rim and the crust. Figure 8 shows a few relatively large nodules, dominated by Cr and O, on the alloy surface. These nodules are interpreted as chromium oxide. Chlorine was mainly found outside the oxide rim, probably being associated with Fe and/or Cr and Al. The base oxide had approximately the same thickness on both alloys, but in the case of alloy Kanthal APMT there was internal oxidation as well, see below.

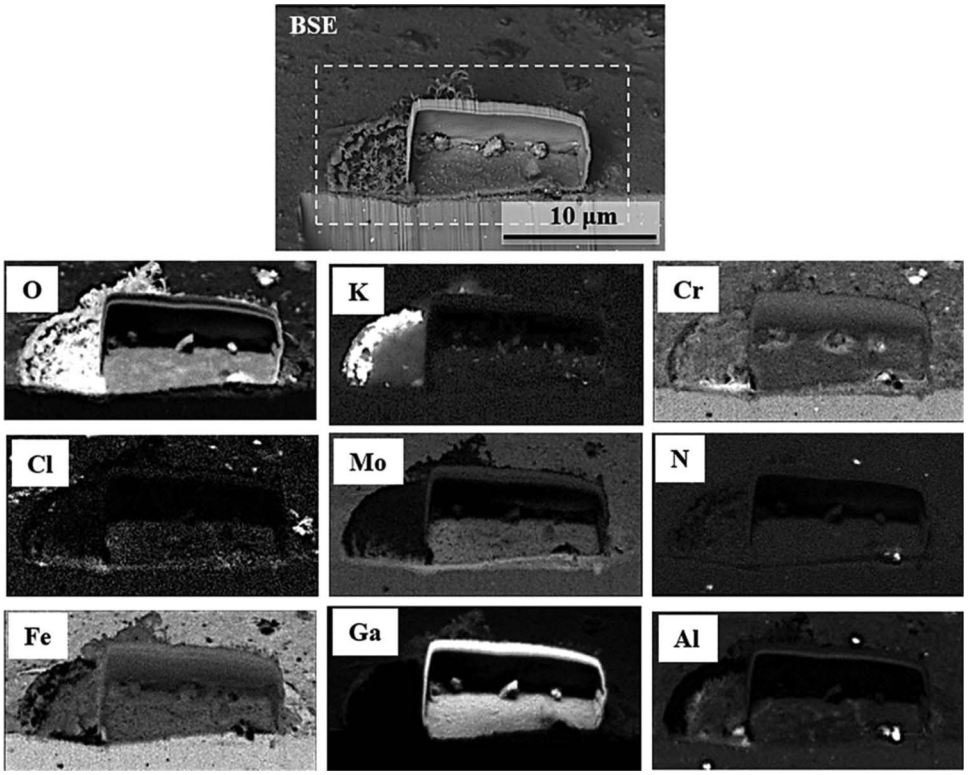

Figure 8. Cross-sectional SEM-EDX maps from Kanthal APMT. (In-situ exposure, lab air, 1 h, 450°C).

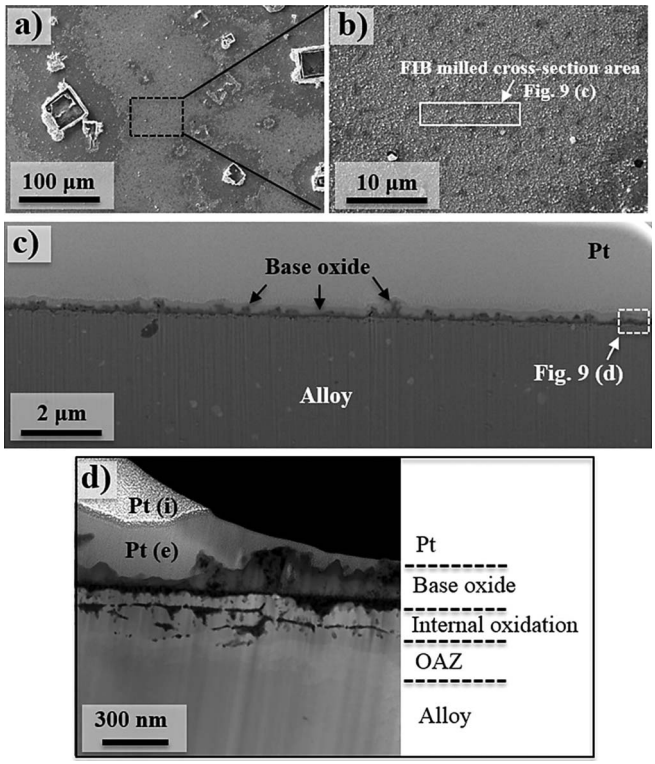

Figure 9. a) Plan view SEM-SE micrograph of the in-situ exposed alloy Kanthal APMT, b) a high-magnification SEM-SE image of the boxed area in Fig. 9a showing the region of Pt deposition and the milling, c) overview SEM-SE micrograph showing a dark oxide scale beneath the brighter Pt-layer from the boxed area in Fig. 8b, and d) STEM-HAADF cross-section image showing the formation of several thin oxide layers. The oxide scale is covered by ion-assisted Pt (i) and electron assisted Pt (e). (In-situ exposure, lab air, 1 h, 450°C).

After Pt-deposition, a FIB milled cross-section was prepared through the thin base oxide on alloy Kanthal APMT, see Figs. 9a and 9b. A SEM-SE micrograph of the FIB-prepared cross-section is shown in Fig. 9c. The base oxide is less even compared to alloy TH1 (compare Fig. 4). Figure 9d shows a STEM-HAADF cross-section micrograph acquired from the boxed area in Fig. 9c. The inner part of the Pt-layer was deposited with the aid of electrons, while the outer (thickest) part was deposited using Ga-ions, generating a difference in contrast within the Pt-layer. The base oxide had a thickness in the range of 50–250 nm and consisted of a top and a bottom layer. In addition to the two-layered base oxide seen in Fig. 9d, there was also evidence for internal oxidation, an almost continuous oxide layer having formed about 100 nm below the base oxide (Fig. 9d).

STEM-HAADF and BF images and STEM-EDX maps of the cross-section are shown in Fig. 10. Pores were observed at the interface between the alloy and the bottom of the base oxide (more clearly seen in the STEM-BF images). Dark areas in the HAADF image indicate the presence of light elements or porosity. The elemental maps in Fig. 10b show that Cr and Fe dominated the top part of the base oxide while the bottom part was porous and mainly consisted of alumina. Also, the semi-continuous oxide layer within the alloy substrate, about 50–100 nm below the two-layered base oxide is seen to consist of alumina. The OAZ was depleted in Cr, Al and Fe. A linescan acquired across the oxide scale and the OAZ corroborated these findings and also showed that small amounts of chlorine were associated with the semi-continuous alumina layer in the alloy. Also, the linescan revealed that the top Cr-Fe oxide layer had a compositional gradient, the Fe/Cr ratio increasing toward the scale/gas interface (see Fig. 10c). Moreover, the Cr-Fe oxide layer was non-uniform with an uneven distribution of Cr, exhibiting strong fluctuations in Cr and Fe contents. In all, the results demonstrated that the alloy exhibited a combination of internal oxidation and chlorination and that it has failed to form a compact and continuous protective scale. The OAZ had a thickness of around 200–300 nm, being thicker than in the case of alloy TH1, which was around 40–80 nm, (see above).

Tube furnace reference exposures.— In order to validate the results from the in-situ ESEM exposures, reference exposures were carried out using a horizontal tube furnace. These exposures were done at 450°C in lab air, the main difference compared with the in-situ exposures being the higher total pressure (1 atm = 760 Torr) and the correspondingly higher partial pressures of O_2 and H_2O.

The surface morphology of the two alloys after 1 hour's exposure is shown in Fig. 11. The appearance of the base oxide was similar to that obtained for the ESEM exposures; a thin, smooth oxide scale with some slightly thicker nodules, compare Figs. 1 and 6 with 11. The main difference was that the amount of KCl remaining after 1 hour in the furnace tube experiment was much greater in the tube furnace exposure. Also, oxide features in the immediate vicinity of the KCl particles were not as well developed and the needle-like crystals observed on alloy TH1 were absent after the tube furnace exposure.

Discussion

ESEM in-situ exposures and imaging.— To investigate high temperature corrosion in-situ in the ESEM, corrosion has to be relatively fast, meaning that the surface morphology should change on a timescale of minutes rather than days. In addition, if a corrosion stimulant is added in the condensed phase (in this case KCl(s)), it has to stay long enough on the surface in order to interact significantly with the material. This can be a problem for substances with high vapour pressure.

Main differences between ESEM oxidation exposures and standard tube furnace exposures include lower total pressure, the interaction of the sample surface with the electron beam and the presence of traces of carbonaceous substances emanating from the vacuum system.[27] In addition, the ESEM oxidation exposures feature less perfect control of sample temperature and flow conditions compared to standard tube furnace exposures. Hence, it becomes necessary to compare the corrosion behavior in the ESEM with conventional furnace exposures at ambient pressure and to verify that the corrosion reaction is not influenced in a major way by artefacts related to the ESEM.

This work shows that the KCl-induced corrosion of the two alumina-forming high temperature alloys selected can be investigated in-situ, in the ESEM, elucidating the dynamics of the phenomena. By continuously recording images during exposure, the oxide scale growth can be monitored in areas in-between, close to, and even on the KCl particles. Also, the consumption of KCl on the surface can be studied.

Reaction of KCl on the surface.— The KCl crystals present at the start of the exposure are rapidly consumed, see e.g. Fig. 1 after 6 minutes exposure of alloy TH1 at 450°C. KCl evaporates in molecular form:

$$KCl\,(s) \rightarrow KCl\,(g) \qquad [1]$$

At the experimental temperature (450°C) the equilibrium pressure of KCl(g) over KCl(s) is only 2.4×10^{-9} bar.[37] The reactions of KCl with water vapour to form HCl(g) + KOH are even less favoured by thermodynamics:

$$KCl\,(s) + H_2O\,(g) \rightarrow KOH\,(g) + HCl\,(g) \qquad [2]$$

$$KCl\,(s) + H_2O\,(g) \rightarrow KOH\,(l) + HCl\,(g) \qquad [3]$$

Thus, the vapour species generated in reactions 2 and 3 have equilibrium pressures of 10^{-11} bars and lower.[37] The rate of volatilization of a substance in vacuum can be estimated, if the equilibrium vapour

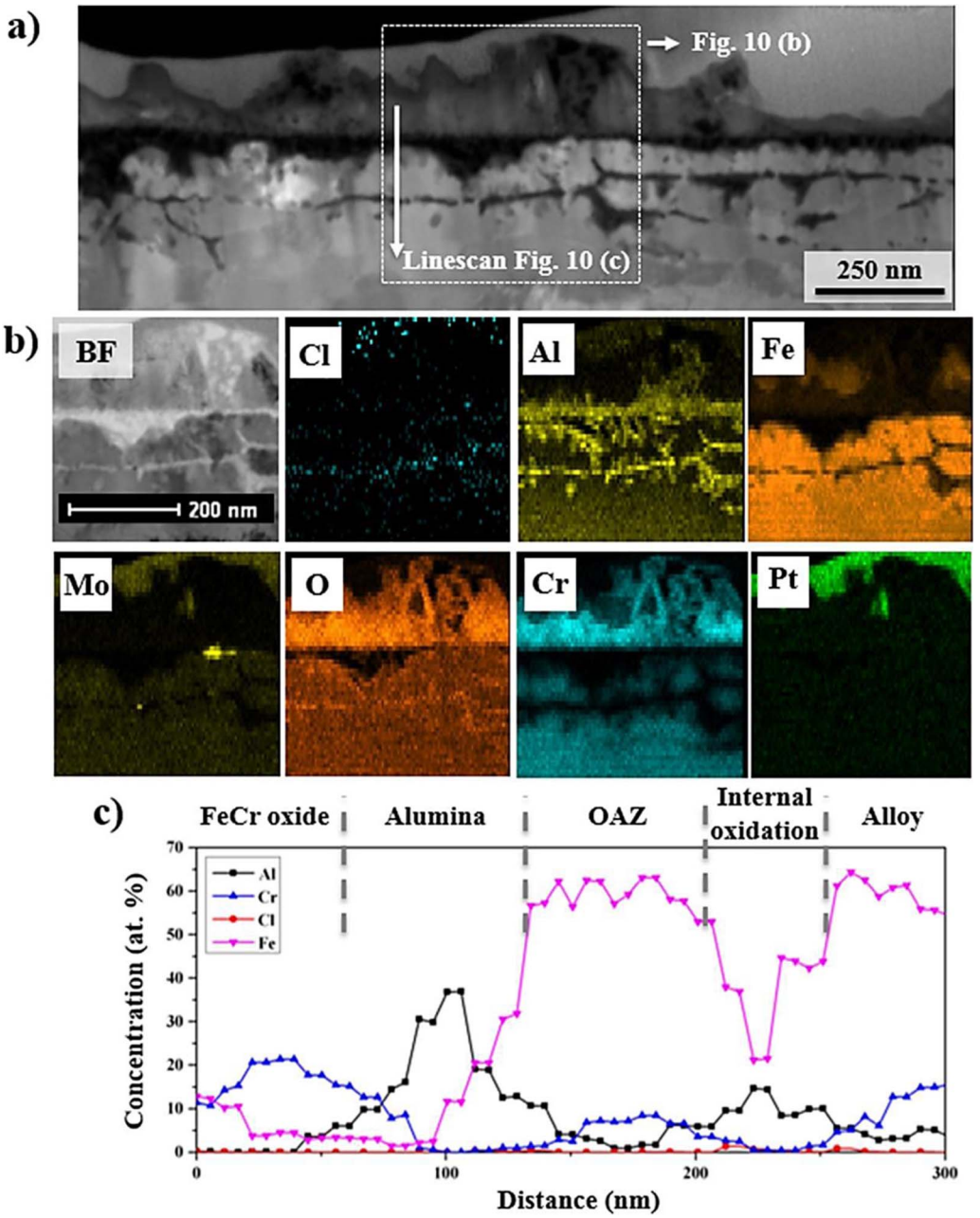

Figure 10. a) STEM-HAADF image acquired from alloy Kanthal APMT, b) STEM-BF image and EDX maps of the boxed area in Fig. 10a, and c) STEM/EDX linescans across the oxide scale and affected area shown by an arrow in Fig. 10a. (In-situ exposure, lab air, 1 h, 450°C).

pressure is known, using the following empirical relation 4.[38]

$$\Gamma_e = 5.84 \times 10^{-2} \sqrt{\frac{M}{T}} P_v \frac{g}{cm^2 s} \quad [4]$$

Where Γ_e is the mass evaporation, P_v is the equilibrium vapor pressure (Torr), T is temperature (°C) and M is the atomic mass. The rate of volatilization of KCl at 450°C in vacuum calculated by 4 becomes 3×10^{-8} g/cm^{2}s. For a $20 \times 10 \times 10$ µm^3 KCl crystal this rate of volatilization corresponds to complete volatilization after about 4.5 h. Hence, the observation that no KCl was left on the surface after 60 minutes (see Fig. 1, 6) implies that the consumption of KCl is mainly due to reaction with the surface.

Working with the corrosion of FeCrNi and FeCrAl alloys in the presence of KCl, O_2 and H_2O,[32–36] reported that potassium chromate formed on the corroding metal surface according to:

$$1/2Cr_2O_3\,(s) + 2KCl\,(s) + 3/4O_2\,(g) + H_2O\,(g) \rightarrow K_2CrO_4\,(s) + 2HCl\,(g) \quad [5]$$
$$(\Delta G^\circ{}_f(450^\circ C) = 80.83 \text{ kJ/Mol})$$

Using the gas composition in the ESEM exposure ($PO_2 = 2 \times 10^{-3}$ bar, $PH_2O = 6 \times 10^{-5}$ bar) and putting $a(Cr_2O_3) = 1$, P(eq) HCl generated by reaction 5 becomes 7.3×10^{-7} bar. It was also reported[32] that in the absence of H_2O, K_2CrO_4 formation was accompanied by the formation of $FeCl_2$, $CrCl_2$ and $AlCl_3$ according to:

$$2KCl\,(s) + 5/4O_2\,(g) + {}^1\!/_2Cr_2O_3\,(s) + Fe\,(s) \rightarrow K_2CrO_4\,(s) + FeCl_2\,(s) \quad [6]$$
$$(\Delta G^\circ{}_f(450^\circ C) = -180.98 \text{ kJ/Mol})$$

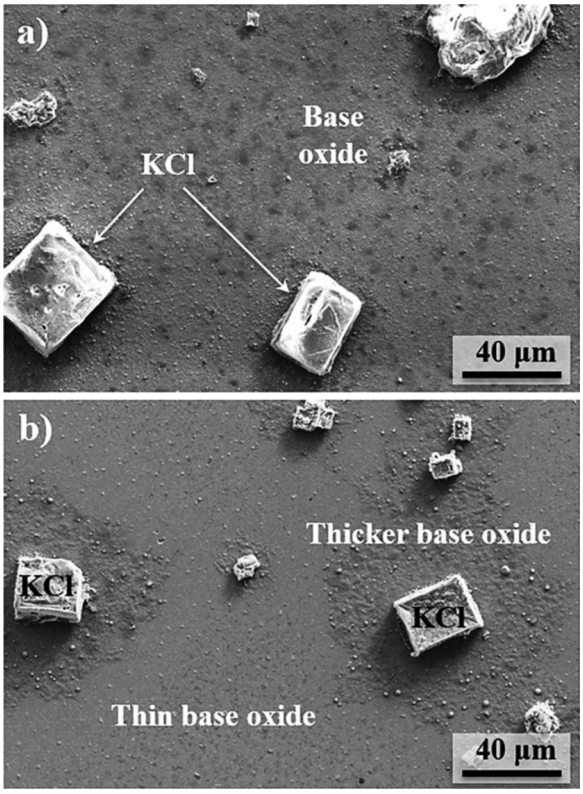

Figure 11. Plan view SEM-SE micrographs of a) alloy TH1 and b) Kanthal APMT. (Reference tube furnace (ex-situ) exposure, lab air, ambient pressure, 1 h, 450°C).

$$2KCl\,(s) + 5/4O_2\,(g) + {}^1\!/_2Cr_2O_3\,(s) + 2/3Al\,(s) \rightarrow K_2CrO_4\,(s) + 2/3AlCl_3\,(l) \quad [7]$$
$$(\Delta G^\circ{}_f(450^\circ C) = -297.88\ \text{kJ/Mol})$$

$$2KCl\,(s) + 5/4O_2\,(g) + {}^1\!/_2Cr_2O_3\,(s) + Cr\,(s) \rightarrow K_2CrO_4\,(s) + CrCl_2\,(s) \quad [8]$$
$$(\Delta G^\circ{}_f(450^\circ C) = -236.81\ \text{kJ/Mol})$$

It may be noted that the equilibrium pressure of HCl in the ESEM environment generated by reaction 5 is more than 100 times larger than P(KCl) generated by reaction 1 and that reactions 6, 7 and 8 are thermodynamically favored. This suggests that the consumption of KCl on the surface of the two alloys is mainly due to a combination of reactions 5 and 6–8.

Accordingly, the present results give ample evidence for the rapid formation of K_2CrO_4 on both alloys (see Fig. 3, 8 and below). Also, chlorides of the main alloying elements were observed both on alloy TH1 (chloride-containing corrosion product needles, see Fig. 3) and on alloy Kanthal APMT (chloride at the scale alloy interface, see Fig. 8). Also, the rapid lateral transport of iron and aluminum ions on the surface of both alloys provides indirect evidence for the presence of $FeCl_2$, $CrCl_2$ and $AlCl_3$ (see below).

General corrosion behavior of TH1 and Kanthal APMT.— Exposure to KCl in an O_2/H_2O environment at a reduced pressure of 6.4×10^{-3} bar (4.8 Torr) at 450°C, was quite corrosive toward both alloys, with copious evidence for corrosion appearing already after 1 hour. In general, the corrosion behavior of alloy TH1 and Kanthal APMT was similar. Far from the KCl particles, both alloys formed a thin base oxide and potassium chromate particles. Also, both alloys formed a lot of corrosion products at the KCl particles, for example the oxide rims and oxide crusts in alloy APMT (Fig. 7) and the oxide shells and oxide crusts in alloy TH1 that replaced the KCl particles (Figs. 2). In the case of alloy TH1, large needle-like crystals formed next to the oxide crusts. In contrast, alloy Kanthal APMT formed porous corrosion product crusts on the outside of the oxide rims. The alloy substrate below the KCl particles was affected by corrosion, forming a sub-micron OAZ, which was depleted in Cr and enriched in Ni (TH1) or Mo (Kanthal APMT), see Figs. 3 and 8. The detrimental effect of KCl on the underlying scale formed on alumina forming alloys is provided in 19 and 21.

The formation of oxide rims and oxide shells.—On both alloys, many KCl crystals were quickly overgrown by oxide (Figs. 1, 6). The rapid consumption of KCl thus left oxide shells (Fig. 2) or rims (Fig. 7) behind that mimicked the shape of the original KCl particles (Fig. 7). The oxide rims and shells were between 0.5 and several microns thick and contained iron, aluminum and some chromium in addition to oxygen (see Figs. 3 and 8).

Similar oxide rims/shells have been reported to form on stainless steel at 500°C and 600°C in the presence of KCl particles (at ambient pressure) in $O_2 + H_2O$,[21,33,39] and $O_2 + H_2O + N_2$ environment.[34,35] Also, an in-situ ESEM paper by T. Jonsson et al.[28] reported that KCl crystals deposited on a low-alloy steel surface were rapidly overgrown by iron oxide agglomerations forming oxide rims and shells in ambient air at 400°C. According to Ref. 28 $FeCl_2$ plays a central role in oxide rim/shell formation. It was proposed that $FeCl_2$ formed by reaction 9 was present at the scale/gas interface:

$$Fe + {}^1\!/_2O_2 + 2KCl \rightarrow FeCl_2 + 2KOH \quad [9]$$

It was argued that $FeCl_2$ formed a melted surface layer on the surface together with KCl, the eutectic temperature in the KCl-$FeCl_2$ system being 355°C.[40] It was postulated that a $FeCl_2$ concentration gradient was set up in the melt, causing iron chloride to diffuse toward the KCl crystals. The formation of iron oxide rims (alloy APMT) and oxide shells (alloy TH1) then results from the spontaneous decomposition of $FeCl_2$ into iron oxide and HCl(g):

$$FeCl_2\,(s) + 1/4O_2\,(g) + H_2O\,(g) \rightarrow {}^1\!/_2Fe_2O_3\,(s) + 2HCl\,(g) \quad [10]$$

($\Delta G^\circ{}_f$ (450°C) = −54.01 kJ/Mol, corresponding to P(eq) HCl = 7.7×10^{-3} bar under the present conditions)

The formation of oxide rims and oxide shells in the present work is explained in a similar way. As the oxide rims/shells formed on the FeCrNiAl and FeCrAl alloys (TH1 and Kanthal APMT) are made up of the oxides of iron, aluminum and chromium, this requires that not only $FeCl_2$, but also $CrCl_2$ and $AlCl_3$ are present in liquid form on the surface. Indeed, $CrCl_2$ does form a low-melting eutectic with KCl, similar to $FeCl_2$.[41] Also, $AlCl_3$ is liquid at the experimental temperature.[42] Hence, it is suggested that $FeCl_2$, $CrCl_2$ and $AlCl_3$ generated by reactions 6–8 form a eutectic melt on the surface together with KCl. Concentration gradients in the surface melt causes $FeCl_2$, $CrCl_2$ and $AlCl_3$ to diffuse toward the KCl crystals. The oxide rim/shell then forms by the decomposition of the chlorides into oxides:

$$AlCl_3\,(melt) + 3/2H_2O\,(g) \rightarrow {}^1\!/_2Al_2O_3\,(s) + 3HCl\,(g) \quad [11]$$

$$CrCl_2\,(melt) + 1/4O_2\,(g) + H_2O\,(g) \rightarrow {}^1\!/_2Cr_2O_3\,(s) + 2HCl\,(g) \quad [12]$$

$$FeCl_2\,(melt) + 1/4O_2\,(g) + H_2O\,(g) \rightarrow {}^1\!/_2Fe_2O_3\,(s) + 2HCl\,(g) \quad [13]$$

The observation that the development of the different corrosion features is faster in the in-situ experiment compared to at ambient pressure (compare Figs. 1, 6 and 11) is tentatively attributed to reactions 11–13 which are expected to be faster in the ESEM, the volatilization of HCl being promoted by the low pressure.

The base oxide.—During the ESEM exposure both alloys formed a thin base oxide between the KCl particles (Fig. 5 and Fig. 10) consisting of a bottom alumina layer and an outer iron chromium oxide

layer. A similar layered base oxide has been reported to form on the melt processed FeCrAl alloy Kanthal AF both in the presence and absence of KCl at 600°C.[15,19] The cross-section STEM-EDX images in Fig. 5 and the cross-section SEM-EDX images in Fig. 8 show potassium chromate particles on the base oxide for both alloys. Chromate formation was commented on above (see Equations 5–8). Fig. 5 reveals that the base oxide on alloy TH1 consists of a continuous bottom alumina layer, covered by iron chromium oxide. The top surface is poor in iron and rich in chromium and potassium, suggesting the presence of potassium chromate. Chlorine has penetrated the alumina layer and formed chlorides with the alloying elements. Beneath the scale there is an OAZ, which is depleted in Cr and Al and enriched in Ni. However, there is no internal oxidation.

The base oxide formed on Kanthal APMT was similar to that formed on alloy TH1, consisting of a bottom alumina layer overlaid by iron chromium oxide (see the linescan in Fig. 10). As expected, the base oxide formed on the Fe-base alloy Kanthal APMT is richer in iron compared to that formed on the Ni-base alloy TH1. Kanthal APMT showed clear evidence of internal oxidation, an almost continuous alumina layer having formed within the alloy (Fig. 9e, Fig. 10). Similar to alloy TH1, chlorine penetrated the external alumina layer on alloy Kanthal APMT. In this case, small amounts of alloying element chlorides were detected at the internal alumina layer. These results imply that the scale formed on alloy TH1 was more protective than that on Kanthal APMT. However, it is cautioned that the long term corrosion behavior cannot be predicted only from the one-hour exposures in the present study.

Growth of alumina layers at "low" temperature.—While α-Al_2O_3 is the thermodynamically stable alumina polymorph, it is reported to not form at the experimental temperature used (450°C). Instead, Al_2O_3 is expected to be present in one of its many metastable forms. Compared to α-Al_2O_3 the metastable aluminas grow faster, being less protective.[43] There are few reports on the early oxidation of FeNiCrAl alloys. Hall et al.[44] reported that a fully protective, continuous alumina layer had formed on alloy TH1 after 24 h in dry and humid atmospheres at 900°C. Josefsson et al.[45] reported that the melt processed FeCrAl alloy Kanthal AF formed alumina-rich protective layers when exposed to O_2 at 500, 600 and 700°C for 168 hours. The oxide film (20, 50 and 130 nm thick, respectively) was dominated by alumina in all cases. While no crystalline oxide was detected at 500°C, crystalline $Cr_{2-x}Fe_xO_3$ was identified at 600°C and $Cr_{2-x}Fe_xO_3$ + α-Al_2O_3 at 700°C. Similarly, Canovic et al. reports that crystalline alumina was not detected on the FeCrAlRE alloy Kanthal AF after 72 h at 600°C in O_2 and in O_2 + H_2O environment.[15] In the present study, attempts to identify the alumina formed on the two alloys by nano-diffraction methods indicated that it was not crystalline.

Formation of protective alumina layers - the role of Cr.—It is well-known that the oxidation properties of alumina-forming alloys are improved by chromium.[46–48] In this regard, Perez et al.[49] reported that the addition of up to 9% chromium in a Fe-30Mn-5Al austenitic stainless steel resulted in less initial oxidation in the temperature range 600–900°C. The beneficial effect of chromium has been explained by the so-called third-element effect (TEE).[50] In the TEE concept, adding a third element C to a binary alloy A-B, the oxygen affinity of C being intermediate between A and B, promotes the transition from internal to external oxidation. Thus, Wagner[51,52] proposed that the third element acts as an oxygen getter during initial oxidation, limiting the inward diffusion of oxygen and allowing the formation of an external B_xO_y layer at a lower concentration of B in the alloy. Additionally, a mixed iron chromium oxide layer with corundum structure can act as a nucleation centre for the formation of α-Al_2O_3. Accordingly, it is suggested that the mixed iron chromium oxide layer plays an important role for the corrosion behavior of the two alloys studied.

It may be noted that while alloy APMT contains more chromium than alloy TH1, the Cr/Fe ratio is higher in alloy TH1 (about 1) than in alloy Kanthal APMT (about 0.3). According to EDX (Figs. 5 and 10), the corresponding elemental ratios in the base oxide on alloy TH1 and Kanthal APMT were about 11 and 2, respectively. It is suggested that the better oxidation resistance of alloy TH1 is due to its higher Cr/Fe ratio and that chromium acts as an oxygen getter at the scale/alloy interface, reducing the inward diffusion of O into the alloy and blocking the internal oxidation of Al. In contrast, the lower Cr/Fe ratio in alloy Kanthal APMT leads to more iron oxide formation in the scale. As a result, there is more oxygen dissolution into the alloy, promoting internal alumina precipitation.

In addition to the shell-like oxide and oxide rim structures which appeared on both alloys, porous oxide crusts and oxide needles formed at the KCl particles on alloy Kanthal APMT and on alloy TH1, respectively. The oxide crusts formed on both alloys consisted of a mixture of Fe-Cr oxide and alumina together with embedded potassium chromate (Kanthal APMT) particles and traces of unreacted KCl (TH1). The composition of the oxide crusts is similar to that of the oxide shells/rims (see Fig. 8). Accordingly, it is suggested that the oxide crusts have formed in a similar way as the oxide shells, i.e., by decomposition of $AlCl_3$, $FeCl_2$ and $CrCl_2$ in a KCl eutectic according to reactions 6–8.

The oxide needles formed on alloy TH1 reached 20 μm in length. According to EDX point analysis and mapping, the needles mainly consisted of Cr_2O_3 together with some iron oxide (See Fig. 3). The iron oxide was enriched at the surface while the interior of the needles was mainly chromium oxide. Based on their composition and shape it is considered that the needles consist of single crystals (whiskers) of Cr_2O_3, Fe_2O_3 and Cr_2O_3 - Fe_2O_3 solid solution. It is suggested that the needles have grown by the decomposition of $CrCl_2$ and $FeCl_2$ in a KCl eutectic according to reactions 12 and 13 and that the traces of KCl and transition metal chloride found on the needles are remnants of the KCl/$CrCl_2$/$FeCl_2$ eutectic. The formation of chromia/hematite needles by decomposition of gaseous $CrCl_2$, $CrCl_3$ and $FeCl_2$ is also possible but is considered less likely because of the low hydrostatic pressure and the continuous pumping out of the gases from the chamber due to low-vacuum set-up. The absence of alumina whiskers is in line with the absence of evidence for crystalline alumina (see above). The observation that oxide needles form on alloy TH1 and not on alloy Kanthal APMT is suggested to be related to the high chromia content in the needles. Thus it is hypothesized that chromia is essential for needle formation and that more chromium chloride is available on the TH1 surface.

Conclusions

- The initial stages of the KCl induced corrosion of a FeCrAl and a FeNiCrAl alloy was successfully studied in the ESEM at 450°C in a lab air environment at 4.8 Torr. Both alloys corroded rapidly and the oxidation morphology changed on the order of minutes.
- The alloys formed oxide crusts and oxide rims (FeCrAl) or oxide shells (FeNiCrAl) around the KCl crystals. The oxide shells/rims mainly consisted of aluminum oxide and iron oxide.
- In addition to the oxide rims/shells and crusts, the FeNiCrAl alloy also formed oxide needles composed of the oxides of iron and chromium. The oxide needles and the oxide rims/shells are suggested to have formed by similar mechanisms involving traces of KCl/$FeCl_2$ KCl/$CrCl_2$ and KCl/$AlCl_3$ melts on the surface. Thus, the alloying element chlorides diffuse in the surface melt toward the KCl crystals where they decompose, forming HCl(g) and the respective oxide.
- Most of the alloy surface was covered by a thin base oxide and potassium chromate nodules. The base oxide was made up of a bottom alumina layer and a top layer consisting of iron chromium oxide.
- While the FeCrAl alloy suffered internal oxidation, i.e. forming alumina precipitates within the alloy, the FeNiCrAl alloy did not. The superior ability of the FeNiCrAl alloy to resist internal oxidation is attributed to the higher Cr/Fe ratio in the alloy and in the oxide scale.
- Both alloys were chlorinated as evidenced by the presence of chlorine at the internal oxide precipitates in alloy APMT and at the scale alloy interface for alloy TH1.

References

1. L. Gustavsson, J. Holmberg, V. Dornburg, R. Sathre, T. Eggers, K. Mahapatra, and G. Marland, "Using biomass for climate change mitigation and oil use reduction," *Energy Policy*, **35**, 5671 (2007).
2. B. Wahlund, J. Yan, and M. Westermark, "Increasing biomass utilisation in energy systems: A comparative study of CO_2 reduction and cost for different bioenergy processing options," *Biomass and Bioenergy*, **26**, 531 (2004).
3. C. Azar, K. Lindgren, and B. A. Andersson, "Global energy scenarios meeting stringent CO_2 constraints - Cost-effective fuel choices in the transportation sector," *Energy Policy*, **31**, 961 (2003).
4. J. Engkvist, N. Israelsson, and U. Bexell, "The initial effect of KCl deposit on alumina scales characterized by ToF-SIMS and AES," *Surf. Inter. Anal.*, **45**, 445 (2013).
5. L. L. Baxter, T. R. Miles, T. R. Miles, B. M. Jenkins, T. Milne, D. Dayton, R. W. Bryers, and L. L. Oden, "The behavior of inorganic material in biomass-fired power boilers: field and laboratory experiences," *Fuel Process Technol.*, **54**, 47 (1998).
6. R. L. Bain, R. P. Overend, and K. R. Craig, "Biomass-fired power generation," *Fuel Process Technol.*, **54**, 1 (1998).
7. B. Jenkins, L. Baxter, T. Miles, and T. Miles, "Combustion properties of biomass," *Fuel Process Technol.*, **54**, 17 (1998).
8. H. Kassman, J. Pettersson, B. M. Steenari, and L. E. Åmand, "Two strategies to reduce gaseous KCl and chlorine in deposits during biomass combustion - Injection of ammonium sulfate and co-combustion with peat," *Fuel Process Technol.*, **105**, 170 (2013).
9. P. Viklund, A. Hjörnhede, P. Henderson, A. Stålenheim, and R. Pettersson, "Corrosion of superheater materials in a waste-to-energy plant," *Fuel Process Technol.*, **105**, 106 (2013).
10. H. Asteman, J. Svensson, M. Norell, and L. Johansson, "Influence of Water Vapor and Flow Rate on the High-Temperature Oxidation of 304L; Effect of Chromium Oxide Hydroxide Evaporation," *Oxid. Met.*, **54**, 11 (2000).
11. C. Pettersson, L. G. Johansson, and J. E. Svensson, "The influence of small amounts of KCl(s) on the initial stages of the corrosion of alloy sanicro 28 at 600°C," *Oxid. Met.*, **70**, 241 (2008).
12. L. Intiso, L. G. Johansson, S. Canovic, S. Bellini, J. E. Svensson, and M. Halvarsson, "Oxidation behavior of Sanicro 25 (42F e22Cr25NiWC uNbN) in O_2/H_2O mixture at 600°C," *Oxid. Met.*, **77**, 209 (2012).
13. S. Enestam, D. Bankiewicz, J. Tuiremo, K. Mäkelä, and M. Hupa, "Are NaCl and KCl equally corrosive on superheater materials of steam boilers?," *Fuel*, **104**, 294 (2013).
14. M. Halvarsson, J. E. Tang, H. Asteman, J. E. Svensson, and L. G. Johansson, "Microstructural investigation of the breakdown of the protective oxide scale on a 304 steel in the presence of oxygen and water vapour at 600°C," *Corros. Sci.*, **48**, 2014 (2006).
15. S. Canovic, J. Engkvist, F. Liu, H. Lai, H. Götlind, K. Hellström, J.-E. Svensson, L.-G. Johansson, M. Olsson, and M. Halvarsson, "Microstructural Investigation of the Initial Oxidation of the FeCrAlRE Alloy Kanthal AF in Dry and Wet O_2 at 600 and 800°C," *J. Electrochem. Soc.*, **157**, C223 (2010).
16. J. Engkvist, S. Canovic, F. Liu, H. Götlind, J. E. Svensson, L. G. Johansson, M. Olsson, and M. Halvarsson, "Oxidation of FeCrAl foils at 500–900°C in dry O_2 and O_2 with 40% H_2O," *Mater. High Temp.*, **26**, 199 (2009).
17. B. A. Pint, "High temperature corrosion of alumina-forming iron, nickel and cobalt-base alloys," *Shreir's Corros.*, 606 (2010).
18. N. Israelsson, K. Hellström, J.-E. Svensson, and L.-G. Johansson, "High-temperature corrosion of an FeCrAl alloy in a waste-fired CHP boiler''. Submitted to *Mater. High Temp.*, (2015).
19. N. Israelsson, J. Engkvist, K. Hellström, M. Halvarsson, J.-E. Svensson, and L.-G. Johansson, "KCl-Induced Corrosion of an FeCrAl Alloy at 600°C in O_2 + H_2O Environment: The Effect of Pre-oxidation," *Oxid. Met.*, **83**, 29 (2015).
20. F. Liu, H. Josefsson, J. E. Svensson, L. G. Johansson, and M. Halvarsson, "TEM investigation of the oxide scales formed on a FeCrAlRE alloy (Kanthal AF) at 900°C in dry O_2 and O_2 with 40% H_2O," *Mater. High Temp.*, **22**, 521 (2005).
21. N. Israelsson, K. A. Unocic, K. Hellström, T. Jonsson, M. Norell, J.-E. Svensson, and L.-G. Johansson, "A Microstructural and Kinetic Investigation of the KCl-Induced Corrosion of an FeCrAl Alloy at 600°C," *Oxid. Met.*, **84**, 105 (2015).
22. F. Liu, H. Götlind, J. E. Svensson, L. G. Johansson, and M. Halvarsson, "Early stages of the oxidation of a FeCrAlRE alloy (Kanthal AF) at 900°C: A detailed microstructural investigation," *Corros. Sci.*, **50**, 2272 (2008).
23. T. Jonsson, B. Pujilaksono, S. Hallström, J. Ågren, J.-E. Svensson, L.-G. Johansson, and M. Halvarsson, "An ESEM in situ investigation of the influence of H_2O on iron oxidation at 500°C," *Corros. Sci.*, **51**, 1914 (2009).
24. B. Pöter, I. Parezanović, and M. Spiegel, "In-situ scanning electron microscopy and electron backscatter diffraction investigation on the oxidation of pure iron," *Mater. High Temp.*, **22**, 185 (2005).
25. B. Schmid, N. Aas, N. Grong, and R. Ødegård, "High-temperature oxidation of iron and the decay of wüstite studied with in situ ESEM," *Oxid. Met.*, **57**, 115 (2002).
26. P. Bruckel, P. Lours, P. Lamesle, and B. Pieraggi, "In situ ESEM investigations of the oxide growth on hot work tools steel: effect of the water vapour," *Mater. High Temp.*, **20**, 551 (2003).
27. M. Esmaily, N. Mortazavi, M. Shahabi-Navid, J. E. Svensson, L. G. Johansson, and M. Halvarsson, "On the capability of in-situ exposure in an environmental scanning electron microscope for investigating the atmospheric corrosion of magnesium," *Ultramicrosco.*, **153**, 45 (2015).
28. T. Jonsson, N. Folkeson, J. E. Svensson, L. G. Johansson, and M. Halvarsson, "An ESEM in situ investigation of initial stages of the KCl induced high temperature corrosion of a Fe-2.25Cr-1Mo steel at 400°C," *Corros. Sci.*, **53**, 2233 (2011).
29. N. Mortazavi, L. Intiso, N. Israelsson, L.-G. Johansson, and M. Halvarsson, "In-situ investigation of the initial stages of KCl-induced corrosion of a chromia-forming steel at 450°C using an environmental scanning electron microscope," CORROSION, In Press.
30. L. A. Giannuzzi and F. A. Stevie, "Introduction to Focused Ion. Springer," (2005).
31. C. A. Volkert and A. M. Minor, "Focused Ion Beam Microscopy and Micromachining," *MRS Bull.*, **32**, 389 (2007).
32. N. Israelsson, K. Hellström, J.-E. Svensson, and L.-G. Johansson, "KCl-Induced Corrosion of the FeCrAl Alloy Kanthal AF at 600°C and the Effect of H_2O," *Oxid. Met.*, **83**, 1 (2014).
33. J. Pettersson, N. Folkeson, L. G. Johansson, and J. E. Svensson, "The effects of KCl, K_2SO_4 and K_2CO_3 on the high temperature corrosion of a 304-type austenitic stainless steel," *Oxid. Met.*, **76**, 93 (2011).
34. T. Jonsson, J. Froitzheim, J. Pettersson, J. E. Svensson, L. G. Johansson, and M. Halvarsson, "Microstructural investigation of the influence of KCl on the corrosion of 304L exposed to 5% O_2+ N_2," *16th Int. Corros. Congr.*, Beijing, China, 6 (2005).
35. T. Jonsson, J. Froitzheim, J. Pettersson, J. E. Svensson, L. G. Johansson, and M. Halvarsson, "The influence of KCl on the corrosion of an Austenitic stainless steel (304L) in oxidizing humid conditions at 600°C: A microstructural study," *Oxid. Met.*, **72**(3–4), 213 (2009).
36. C. Pettersson, J. Pettersson, H. Asteman, J. E. Svensson, and L. G. Johansson, "KCl-induced high temperature corrosion of the austenitic Fe-Cr-Ni alloys 304L and Sanicro 28 at 600°C," *Corros. Sci.*, **48**, 1368 (2006).
37. "FactSage.com - Introduction to FactSage.," [Online]. Available: http://www.crct.polymtl.ca/factsage/fs_general.php.
38. M. Ohring, "Materials science of thin films, second edition - deposition and structure," (2001).
39. C. Proff, T. Jonsson, C. Pettersson, J. E. Svensson, L. G. Johansson, and M. Halvarsson, "Microstructural investigation of the KCl-induced corrosion of the austenitic alloy Sanicro 28 (35Fe27Cr31Ni) at 600°C," *Mater. High Temp.*, **26**, 113 (2009).
40. E. M. Levin, H. F. McMurdie, and C. R. Robbins, "Phase diagrams for ceramists," (1964).
41. T. B. Massalski, "Binary alloy phase diagrams," ASM International (1990).
42. I. Barin and G. Platzki, "Thermochemical data of pure substances," VCH (1995).
43. P. Kofstad, "High Temperature Corrosion," (1988).
44. J. Hall, K. Hellström, J.-E. Svensson, M. Norell, M. Lundberg, T. Helander, and L.-G. Johansson, "The Initial Oxide Scale Development on a Model FeNiCrAl Alloy at 900°C in Dry and Humid Atmosphere: A Detailed Investigation," *Oxid. Met.*, **82**, 225 (2014).
45. H. Josefsson, F. Liu, J. E. Svensson, M. Halvarsson, and L. G. Johansson, "Oxidation of FeCrAl alloys at 500–900°C in dry O_2," *Mater. Corros.*, **56**, 801 (2005).
46. N. Birks, G. H. Meier, and F. S. Pettit, "Introduction to the high-temperature oxidation of metals," Cambridge University Press (2006).
47. I. A. Kvernes and P. Kofstad, "The oxidation behavior of some Ni-Cr-Al alloys at high temperatures," *Metall. Trans.*, **3**, 1511 (1972).
48. C. H. Lund and H. J. Wagner, "Oxidation of nickel and cobalt-base superalloys," (1965).
49. P. Pérez, G. Garcés, F. J. Pérez, C. Gómez, and P. Adeva, "Influence of Chromium Additions on the Oxidation Resistance of an Austenitic Fe–30Mn–5Al Alloy," *Oxid. Met.*, **57**, 339 (2002).
50. F. H. Stott, G. C. Wood, and J. Stringer, "The influence of alloying elements on the development and maintenance of protective scales," *Oxid. Met.*, **44**, 113 (1995).
51. C. Wagner, "Passivity and inhibition during the oxidation of metals at elevated temperatures," *Corros. Sci.*, **5**, 751 (1965).
52. C. Wagner, "Formation of Composite Scales Consisting of Oxides of Different Metals," *J. Electrochem. Soc.*, **103**, 627 (1956).